# nature physics

**Article** 

https://doi.org/10.1038/s41567-023-02307-w

# Discrete degeneracies distinguished by the anomalous Hall effect in a metallic kagome ice compound

Received: 25 September 2022

Accepted: 26 October 2023

Published online: 10 January 2024



K. Zhao  $lacktriangledown^{1,2} ootimes$ , Y. Tokiwa $^{1,3}$ , H. Chen  $lacktriangledown^{4,5} ootimes \&$  P. Gegenwart  $lacktriangledown^{1} ootimes$ 

In magnetic crystals, despite the explicit breaking of time-reversal symmetry, two equilibrium states related by time reversal are always energetically degenerate. In ferromagnets, this time-reversal degeneracy is reflected in the hysteresis of the magnetic field dependence of the magnetization and, if metallic, in that of the anomalous Hall effect (AHE). Under time-reversal, both these quantities change signs but not their magnitude. Here we show that a time-reversal-like degeneracy appears in the metallic kagome spin ice HoAgGe when magnetic fields are applied parallel to the kagome plane. We find vanishing hysteresis in the field dependence of the magnetization at low temperature, but finite hysteresis in the field-dependent AHE. This suggests the emergence of states with nearly the same energy and net magnetization but different sizes of the AHE and of the longitudinal magnetoresistance. By analysing the experimental data and a minimal tight-binding model, we identify a time-reversal-like operation connecting these near-degenerate states, which is related to the non-trivial distortion of the kagome lattice in HoAgGe. Our work demonstrates the diagnostic power of transport phenomena for identifying hidden symmetries in frustrated spin systems.

Geometrically frustrated spin systems are a promising platform for novel states of matter  $^{1-7}$ . Although magnetic neutron diffraction and magnetometry measurements are direct probes on the spin sector  $^{6,7}$  when the systems of study are sufficiently conductive, electric transport can often provide an enlightening perspective for understanding exotic spin ordering and its consequences  $^{8-12}$ . This is especially the case when the transport coefficients can be directly related to symmetries of the spin order  $^{13-23}$ . A well-known example is the anomalous Hall effect (AHE) observed in pyrochlore iridate  $\text{Pr}_2\text{Ir}_2\text{O}_7$ , which provides evidence of time-reversal symmetry breaking despite the absence of long-range magnetic ordering  $^{10}$ .

As a fundamental discrete symmetry operation, time-reversal plays a particularly important role in magnetic crystals. Adding time-reversal to space group operations establishes magnetic space

groups which allow systematic classification and investigation of magnetic phases. Governed by the basic principles of quantum mechanics, almost all measurable physical quantities have definite transformation properties under time-reversal, which can often provide system-independent predictions. For example, for magnetic phases that break the time-reversal symmetry, two states related by time-reversal are energetically degenerate (a macroscopic manifestation of Kramers theorem). If the magnetic phase is characterized by a non-zero net magnetization, the two phases must have mutually antiparallel net magnetization of same size, and if the phase displays the AHE<sup>8,9</sup>, the AHE must also have opposite signs but same size in the two time-reversal-related states, a consequence of Onsager reciprocity relations<sup>24-26</sup>. Recently, theory and experiment have demonstrated that in certain non-collinear antiferromagnets the AHE can distinguish

<sup>1</sup>Experimentalphysik VI, Centre for Electronic Correlations and Magnetism, University of Augsburg, Augsburg, Germany. <sup>2</sup>School of Physics, Beihang University, Beijing, China. <sup>3</sup>Advanced Science Research Center, Japan Atomic Energy Agency, Tokai, Japan. <sup>4</sup>Department of Physics, Colorado State University, Fort Collins, CO, USA. <sup>5</sup>School of Advanced Materials Discovery, Colorado State University, Fort Collins, CO, USA. ☑e-mail: kan zhao@buaa.edu.cn; huachen@colostate.edu; philipp.gegenwart@physik.uni-augsburg.de

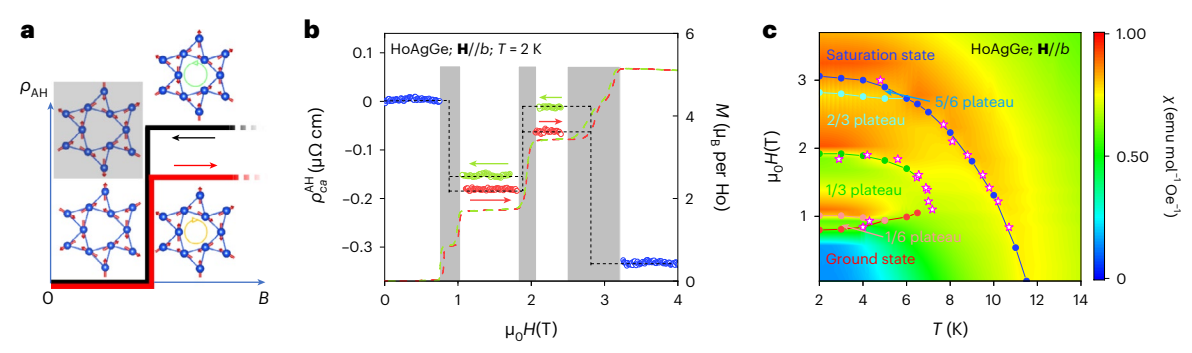


**Fig. 1**| **Time-reversal-like degeneracies in field-induced plateau phases of HoAgGe. a**, Illustration of the finite-field hysteresis of the anomalous Hall resistivity size due to emergent time-reversal-like degenerate states. The two states on the finite-field plateau are  $S_{1/3}$  (top right) and  $S'_{1/3}$  (bottom right); these are described in the text. Depicted at the left are the two degenerate time-reversal partners of the kagome ice ground state (one greyed out for better contrast) which have zero AHE. **b**, Open circles display the anomalous part  $\rho_{ca}^{AH}$  (constantin-field) of the Hall resistivity  $\rho_{ca}$  (current along c, voltage along a) of HoAgGe under  $\mathbf{H}//b$  at 2 K (see details in Supplementary Fig. 31), through subtracting the

ordinary field-linear Hall part, with dashed lines linking the  $\rho_{ca}^{AH}$  plateau values and red and green arrows indicating increasing and decreasing field. Dashed coloured lines display the corrected magnetization M after subtracting an H linear term (see details in Supplementary Fig. 26), with the grey regions indicating the transitions between different magnetic plateaus and  $\mu_B$  standing for Bohr magneton.  $\mathbf{c}$ , The H–T phase diagram of HoAgGe under  $\mathbf{H}//b$  as derived from magnetization M (filled circles) and  $C_{mag}$  and  $I_{mag}$  (empty stars) measurements, with the colour coding representing the magnetic susceptibility (see text).

time-reversal symmetry breaking even though net magnetization is vanishing, although the AHE for the two time-reversal-related states still has the same size  $^{13-23}$ . In this work, however, we show it is possible to use the AHE and the closely related longitudinal magnetoresistance (MR) $^{24,27,28}$  to distinguish near-degenerate states related by an emergent discrete symmetry operation  $\mathcal X$  in a metallic kagome spin ice compound  $^{29-39}$  HoAgGe under finite magnetic fields parallel to the kagome plane. Different from time-reversal, net magnetization (excluding the Berry-curvature-related orbital magnetization  $^{25,40-42}$ ) is unchanged under  $\mathcal X$ , while the AHE and the MR take changed values (Fig. 1a,b).

HoAgGe is an intermetallic compound consisting of stacked kagome lattices with non-trivial distortion formed by Ho<sup>3+</sup>ions<sup>43</sup>. Considering the Ho<sup>3+</sup> ions alone, the distortion reduces the  $D_{6h}$  symmetry of the kagome lattice to  $D_{3h}$ , but does not change the local easy axes of the Ho<sup>3+</sup> moments. The strong local easy-axis anisotropy, together with ferromagnetic nearest-neighbour coupling of the Ho<sup>3+</sup> moments, leads to '1-in-2-out' or '2-in-1-out' ice rules on the kagome lattice<sup>29-39</sup>; the massive degeneracy resulting from the ice rules is weakly lifted by further-neighbour interactions of the Ruderman-Kittel-Kasuya-Yosida type, leading to a  $\sqrt{3} \times \sqrt{3}$  ground state of the dipolar kagome ice below 4 K through a partially ordered phase with decreasing temperature<sup>43</sup>. Interestingly, at low temperatures the magnetization versus external magnetic fields parallel to the kagome plane exhibits a series of plateaus, due to the competition between the Ho<sup>3+</sup> moments' coupling with the fields and the further-neighbour interactions among them<sup>43</sup>. In this work we show that, partly due to the non-trivial distortion of the kagome lattice in HoAgGe (refs. 44,45), a time-reversal-like symmetry operation x as introduced above becomes effective on the magnetic plateaus.

# Contrasting hysteretic behaviour of the AHE, MR and magnetization

HoAgGe crystals were cut into different shapes for magnetic and transport measurements with the demagnetization correction considered (see Methods for details). As shown in Supplementary Fig. 2, the demagnetization correction enables quantitative comparison between measurements on differently shaped crystals. Figure 1c displays a phase diagram of HoAgGe under  $\mathbf{H}//b$  ( $\mathbf{H}$  along b) based on magnetic susceptibility  $\chi$ , magnetic specific heat  $C_{\text{mag}}$  and magnetic Grüneisen parameter  $\Gamma_{\text{mag}}$ . The colour coding in Fig. 1c is based on low-temperature magnetic susceptibility (Supplementary Fig. 4). Metamagnetic transitions into the two lower-field states labelled by 1/3 and 2/3 plateaus

first appear below about 7 K (Supplementary Fig. 3), where the fraction means the ratio between the net magnetization on a given plateau and that in the saturated state. These values can be understood by enforcing the kagome ice rules in a  $\sqrt{3} \times \sqrt{3}$  unit cell. A 1/6 plateau, with a magnetic configuration that is still unclear at the moment, is observed around 4 K (Supplementary Fig. 4). Between 1 T and 2 T, the sharp peak in  $C_{\text{mag}}$  around 10 K marks the transition from the paramagnetic phase to a partial-ordered phase presumably similar to that under zero field, while the broad peak around 7 K corresponds to the transition into a low-temperature metastable phase (1/3 plateau) with Am'm2' symmetry (Fig. 1a and Supplementary Fig. 12c,d). Above 2 T, the sharp peak in  $C_{\text{mag}}$  and  $I_{\text{mag}}$  around 8 K marks the transition from the paramagnetic state to another metastable state (2/3 plateau) with Am'm2' symmetry. The intermediate region between the two phase boundaries is expected to consist of both P-6'm2' and Am'm2' symmetry components. The metamagnetic transition into the saturated state is accompanied by the disappearance of the magnetic vector (1/3, 1/3, 0) in neutron data, with the magnetic unit cell becoming the same as the structural unit cell. (See Supplementary Fig. 5 for other thermodynamic data.)

Figure 2 summarizes field- and temperature-dependent magnetotransport data with  $\mathbf{H}//b$  (see Supplementary Figs. 1, 6, 7, 8 and 9 for details). Through careful analyses of the transport data, the raw  $R_{ca}$  signal of our Hall devices is found to involve admixtures from the longitudinal channel due to effective misalignments of the Hall and/ or current leads that are inevitable in our small devices. Nonetheless, the intrinsic Hall signal can still be faithfully obtained (see in-depth discussion in Supplementary Notes 1 and 2) from the raw  $R_{ca}$  data after proper antisymmetrization. The Hall resistivity  $\rho_{ca}$  is measured with current along c and voltage along a. When H < 3.2 T (dashed line in Fig. 2a), both the Hall resistivity and the MR show clear changes at the metamagnetic transitions. The MR also has a pronounced jump at the 1/6 plateau at 2 K. At 2 K,  $\rho_{ca}$  increases with the field despite the sudden changes at the metamagnetic transitions. At 3 T, when the system transitions to the saturated state,  $\rho_{ca}$  changes rather abruptly with its sign also reversed. Such a feature becomes less pronounced and shifts to lower fields with increasing temperature and eventually disappears at about 11 K, in agreement with Fig. 1c. Previous density functional theory calculations (see Supplementary Fig. S20 of ref. 43) indicate that HoAgGe has multiple bands crossing the Fermi energy in the paramagnetic state, which is consistent with a nonlinear-in-H Hall resistivity at 50 K, shown in Supplementary Fig. 15a. The sign change of  $\rho_{ca}$  around 3 T shown in Fig. 2 may therefore be related to substantial

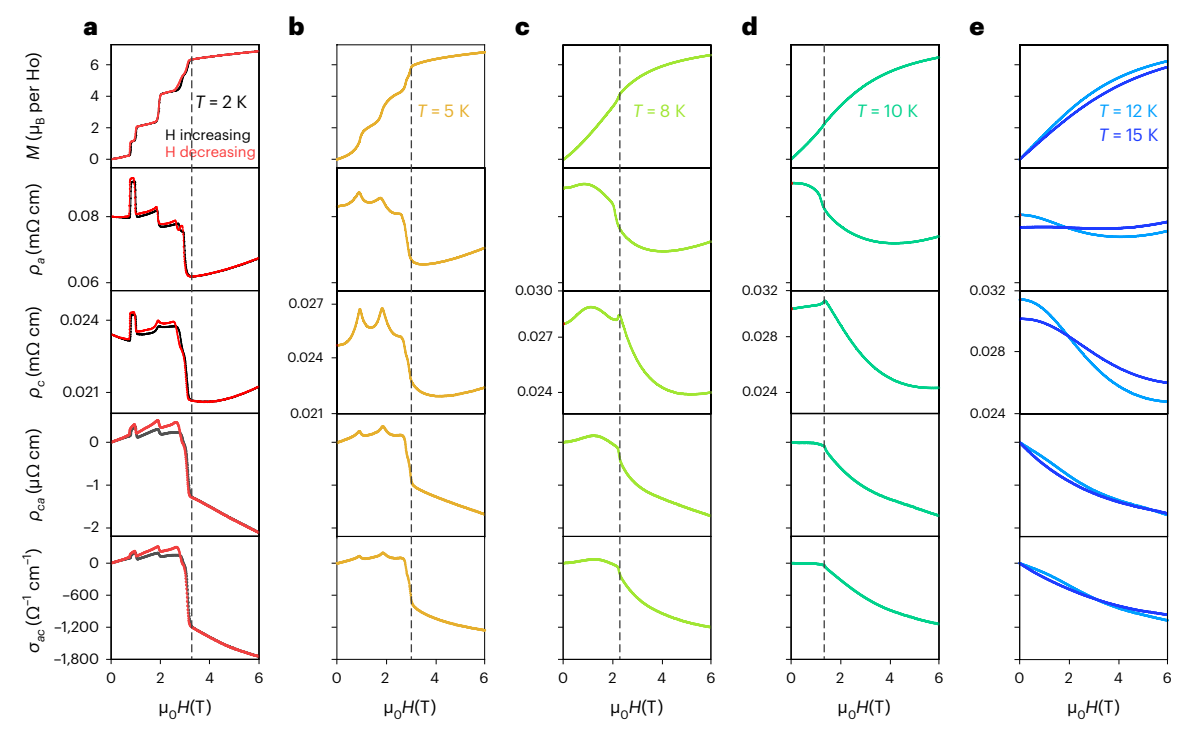


**Fig. 2** | **Magnetic and transport properties of HoAgGe. a**-**e**, For **H**//*b*, the magnetization *M*, the *a*-axis MR  $\rho_a$ , the *c*-axis MR  $\rho_c$ , the Hall resistivity  $\rho_{ca}$  (current along *c*, voltage along *a*) and conductivity  $\sigma_{ac}$  obtained as  $\sigma_{ac} = \rho_{ca}/(\rho_a \rho_c)$  (valid when  $\rho_{avc} \gg \rho_{ca}$ ) are displayed at 2 K (**a**), 5 K (**b**), 8 K (**c**), 10 K (**d**) and 12 K and 15 K (**e**). Dashed lines indicate the saturation fields.

changes of the band structure near the Fermi energy driven by the magnetic order change. The similar trends between the Hall and MR signals at the metamagnetic transitions are likely caused by the same mechanisms contributing to both being affected by the transitions. One example is that the transport relaxation time that controls both the extrinsic AHE and the MR is approximately proportional to the inverse of the density of states at the Fermi energy, which can change abruptly at the metamagnetic transitions.

More interestingly, Fig. 2 shows that at 2 K, the magnetotransport data have clear hysteresis for the 1/3 and 2/3 plateaus, in contrast to the indiscernible hysteresis in the magnetization versus field curves (Supplementary Fig. 26). The hysteresis also persists through the whole 1/3 and 2/3 plateaus rather than just appearing near the metamagnetic transitions. In the middle of each plateau, the physical observables (magnetization, transport coefficients, etc.) have weak dependences on magnetic fields, suggesting that the magnetic order is substantially uniform (more evidence and discussion on this are given below). The hysteretic behaviour of the Hall and MR signals, together with the same critical field values of the metamagnetic transitions at the two halves of the hysteresis loop, strongly indicates the existence, at these temperatures, of at least two degenerate states with the same magnetization on each plateau when H is between 1 T and 3 T.

To show that the hysteresis of the transport data is inseparable from the finite-magnetic-field ordering derived from the  $\sqrt{3} \times \sqrt{3}$  ground state, we directly compare the thermodynamic and transport data versus  $\mathbf{H}//b$  at two temperatures (8 K and 3 K) in Fig. 3. At 8 K (Fig. 3a), when there is only one metamagnetic transition to the saturated state, there is one sharp peak in magnetic specific heat, with position that agrees with the zero-crossing of  $\Gamma_{\text{mag}}$ , due to the entropy accumulation at the phase boundary between the partial-ordered phase and the fully saturated phase. Indeed, the calculated magnetic entropy difference displays a sharp peak and decreases upon further raising magnetic field. The  $\rho_{ca}$  data at 8 K display no hysteresis. At 3 K (Fig. 3b), when the  $\sqrt{3} \times \sqrt{3}$  ground state is realized at zero field, the

three metamagnetic transitions separating 1/3 plateau, 2/3 plateau and the saturation state with their adjacent states are clearly observed in the behaviours of  $C_{\text{mag}}$ ,  $\Gamma_{\text{mag}}$  and magnetic entropy difference  $\Delta S_{\text{mag}}$ .

## The c-axis spin order around 2.5 K

Figure 4a shows the results for magnetic susceptibility  $\chi(T)$  down to 1.8 K with denser data points as compared to Fig. 1A of ref. 43. Besides the sharp peak at 11.8 K and the broad peak at about 7 K, another anomaly appears at 2.5 K, for both  $\mathbf{H}//b$  and  $\mathbf{H}//c$  under 500 Oe. The isothermal out-of-plane magnetization for HoAgGe at 2 K is shown in Fig. 4b. Distinct from the behaviour at 3 K and 4 K, the dM/dH curve exhibits a zero-field peak and an anomaly at approximately 1.1 T at 2 K (ref. 46). Correspondingly, in Fig. 4c, the MR  $\rho_a$  shows an anomaly around 1.1 T at 2 K under  $\mathbf{H}//c$ , with a hump feature centred around 7 T. Besides the anomaly at approximately 1.1 T, the Hall resistivity  $\rho_{ab}$  deviates from the linear behaviour above 10 T, which likely originates from the non-saturating magnetization for  $\mathbf{H}//c$  under high fields.

The above observations suggest that the c-axis components of Ho spins have a dominant antiferromagnetic interaction and become ordered at about 2.5 K under weak magnetic fields. A possible order is the  $\sqrt{3} \times \sqrt{3}$  ground state of the antiferromagnetic kagome Ising model with further-neighbour interactions of ref. 30, considering the consistent (1/3, 1/3, 0) ordering vector from our low-temperature neutron data (Supplementary Fig. S8 in ref. 43). The dM/dH anomaly at about 1.1 T is understood as a longitudinal-field-induced transition in the antiferromagnetic kagome Ising model. Below, we focus on the metastable phases driven by fields in the ab plane, which have been more clearly understood.

# Time-reversal-like degeneracy with different AHE and MR size

The experimental data above suggest that there exist at least two near-degenerate states on the 1/3 and 2/3 plateaus at low temperatures. First, we focus on the 1/3 plateau. Our previous elastic neutron-scattering

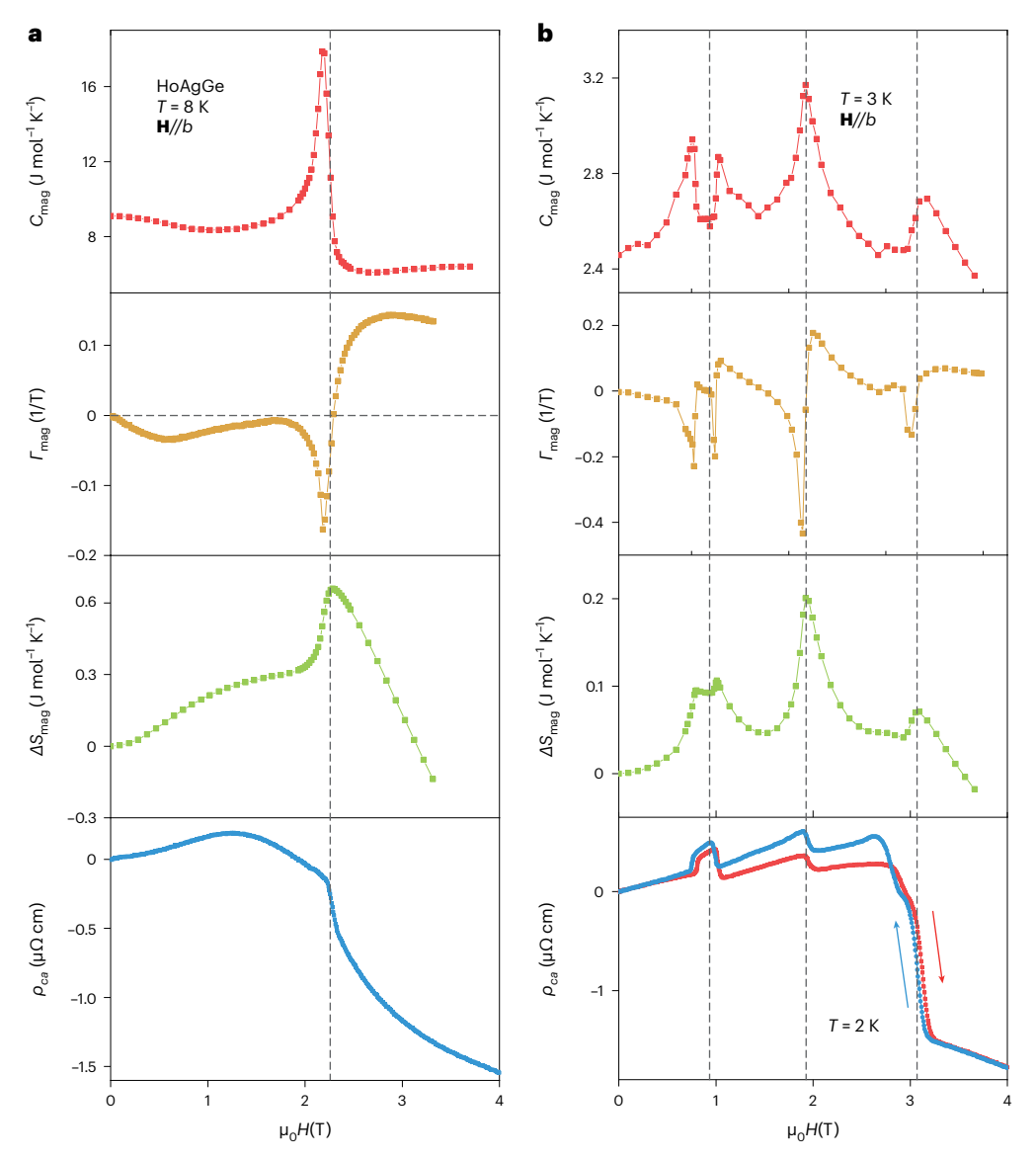


Fig. 3 | Thermodynamic measurements of HoAgGe in comparison with the Hall data. a,b, Field dependence of magnetic specific heat  $C_{\text{mag}}$ , magnetic Grüneisen parameter  $\Gamma_{\text{mag}}$ , magnetic entropy difference  $\Delta S_{\text{mag}}$  and Hall resistivity  $\rho_{ca}$  of HoAgGe at 8 K (a) and 3 K (2 K for Hall resistivity  $\rho_{ca}$ ) (b) under  $\mathbf{H}//b$ .

experiments in ref. 43 suggest that besides the state depicted at the top of Fig. 1a (denoted by  $S_{1/3}$ ; also see Supplementary Fig. 12c), there exists another ice-rule state  $S'_{1/3}$  (Supplementary Fig. 12d) equivalent to the state depicted below  $S_{1/3}$  in Fig. 1a, with the same net magnetization and the same refinement factors (Supplementary Fig. 13). An exhaustive search for all  $\sqrt{3} \times \sqrt{3}$  ice-rule states with the same net magnetization confirmed that  $S_{1/3}$  and  $S'_{1/3}$  are the only distinct states on the 1/3 plateau. Figure 5a shows that the two states can be visualized as a 6-spin ring with opposite chiralities (or toroidal moments)47 enclosed in a larger 3-spin triangle in a 2-in-1-out state.  $S_{1/3}$  and  $S'_{1/3}$ are distinct since they cannot be made equivalent by any operations in their magnetic space group Am'm2'. Moreover, they have the same energy, based on the classical spin model in ref. 43, which involves up to 4th neighbour exchange couplings and dipolar interactions among the Ho spins (Supplementary Note 8), even with symmetry-allowed Dzyaloshinski-Moriya interaction and canting taken into account (Supplementary Note 10).

To see whether  $S_{1/3}$  and  $S'_{1/3}$  can have different AHE, we constructed a minimal tight-binding model respecting the symmetries of HoAgGe and directly calculated the intrinsic contribution to the anomalous Hall

conductivity (AHC). The minimal model (Supplementary Note 6) describes s-electrons hopping between nearest-neighbouring Ho sites subject to local exchange fields parallel to the ordered Ho moments and to spin-orbit coupling determined by the inversion symmetry breaking with respect to the nearest-neighbour bond centres. Surprisingly, despite the complex lattice structure and magnetic order, the band structures for  $S_{1/3}$  and  $S'_{1/3}$  are completely identical (Fig. 5c). While this is partly due to the minimal nature of the model (Supplementary Note 7 and Fig. 20), the exact degeneracy of the Bloch band structures implies non-trivial symmetry relations between  $S_{1/3}$  and  $S'_{1/3}$ , which are discussed below. What is more interesting, however, is that the two states generally have different Berry curvatures (summed over occupied bands) at the same positions in the Brillouin zone (Fig. 5c). Consequently, integrating the Berry curvature over the Brillouin zone gives different intrinsic AHC for  $S_{1/3}$  and  $S'_{1/3}$  (Fig. 5d). The same effect also results in the two states having differences in other Berrycurvature-related quantities, such as the linear magnetoconductivity (Fig. 5c,e) and the orbital magnetization (Fig. 5a,c,f).

We next turn to the 2/3 plateau, noting that if assuming a vanishing *c*-axis component for the Ho spins, there is only one ice-rule state

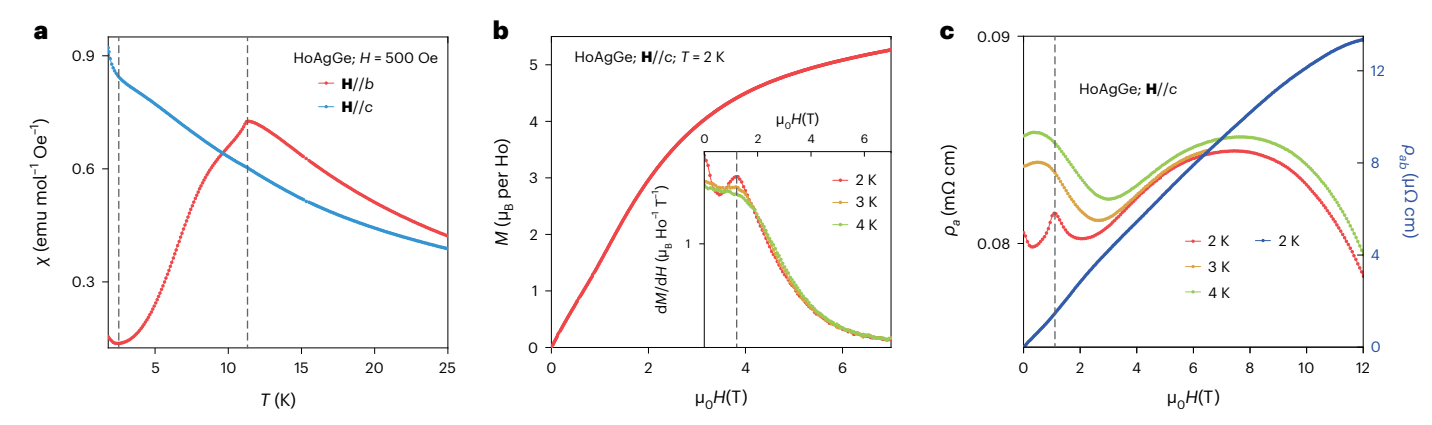


**Fig. 4** | **Magnetic and transport properties of HoAgGe under H**//c. a, Magnetic susceptibility of HoAgGe under **H** along c and b axes from 25 K to 1.8 K. b, The magnetization M under **H**//c at 2 K, with dM/dH curves below 4 K as inset. c, The a-axis MR  $\rho_a$  below 4 K and the Hall resistivity  $\rho_{ab}$  (current along a, voltage along b) at 2 K under **H**//c

compatible with the Am'm2' symmetry. However, based on the experimental data in Fig. 4, we propose two possible 2/3 plateau states ( $S_{2/3}$  and  $S'_{2/3}$ , illustrated in Fig. 5b; see also Supplementary Fig. 12e), which are distinct due to the c-axis spin order and are also related by  $\mathcal{X}$ . The specific c-axis spin order is the ground state of the antiferromagnetic Ising model mentioned above. Critically,  $S_{2/3}$  and  $S'_{2/3}$  have different AHC, MR and orbital magnetization (Fig. 5d–f), although the total energies and band structures are still the same (Supplementary Note 9 and Fig. 22). As discussed below, the c-axis spin order also provides a natural explanation for the kinetic separation between the near-degenerate states across the transition between the 1/3 and 2/3 plateaus.

# Origin of the AHE size difference

To understand why the operation  $\mathcal{X}$  preserves the band structure but not the AHE, we first note that it is not only that  $S_{1/3}$  and  $S'_{1/3}$  ( $S_{2/3}$  and  $S'_{2/3}$ , as well; the subscripts are omitted below unless noted) cannot be made equivalent by operations in their symmetry group Am'm2', but they also cannot be connected by any magnetic space group operations. This indicates that  $\mathcal{X}$  must involve non-trivial operations beyond those in standard magnetic space groups and also implies the possibility of  $\mathcal{X}$  changing the AHE sizes 48 since otherwise the AHC would transform as a pseudovector with fixed length. In our system, x can be concisely represented by  $R_h^{\pi} \mathcal{D}$ , where  $R_h^{\pi}$  is a usual  $\pi$ -rotation about the b axis by  $\pi$  on both orbital and spin degrees of freedom and  $\mathcal{D}$  is a special operation that reverses the distortion of the lattice but keeps the spin degrees of freedom untouched (Fig. 5a; see also Fig. 1a). We stress that the use of  $\mathcal{D}$  is only to facilitate the discussion of the relationship between S and S'. The actual magnetic transitions involving them are not accompanied by any structural distortion reversal. In the paramagnetic state,  $\mathcal{D}$  is equivalent to a vertical mirror parallel to the b axis, or a  $\pi$ -rotation about the c axis, but cannot be represented by a standard magnetic space group operation when the magnetic order on the 1/3 or 2/3 plateaus is in place. Note that distortion reversal has been suggested for inclusion as an additional 'colour symmetry' operation in crystalline space groups 44,45. In non-magnetic crystals, however, distortion reversal can usually be made equivalent to other space group operations, such as mirror reflection, which transform physical observables in a well-defined manner. The effect of  $\mathcal{D}$  on physical quantities such as the Hamiltonian and the AHE needs to be analysed case-by-case due to its separate actions on orbital and spin degrees of freedom. It also does not necessarily lead to exact degeneracy, in contrast to magnetic space group operations. In Supplementary Note 7, we proved that  $\mathcal{D}$  leaves all terms in our tight-binding model invariant except for changing the sign of the crystal momentum along c, thereby

time-reversal-like. Thus,  $\mathcal{X}=R_b^{\pi}\mathcal{D}$  keeps the band structure invariant additionally due to the time-reversal plus  $R_a^{\pi}$  symmetry in Am'm2'. We also proved that the classical spin model of HoAgGe, including Heisenberg, dipolar and Dzyaloshinski–Moriya interactions, gives identical energies for  $S_{1/3}$  and  $S'_{1/3}$  (Supplementary Notes 8 and 10).

The reason the size of the AHC is not invariant under  $\mathcal X$  is more subtle. In Supplementary Note 7 we showed that  $\mathcal D$  critically changes the Berry connection, or the position operator's matrix elements between Bloch states, due to the shift of sublattice positions under  $\mathcal D$ , which changes the Berry curvature of occupied states and hence the AHC. Such a contribution is a manifestation of the fact that the Berry curvature encodes geometric information of the Bloch wavefunctions beyond the band structure. We note that this mechanism will generally be relevant in structurally distorted magnetic systems in which the distortion reversal operation is not equivalent to a magnetic space group operation.

Because of their different Berry curvatures, S and S' have additional properties that differ in the two states, such as the orbital magnetization and the (linear) longitudinal magnetoconductivity (Fig. 5c-f), which depend on the Berry curvature, because it modifies the governing semiclassical equations of motion. On the one hand, the different linear MR serves as an explanation of the hysteresis in the longitudinal resistivity of HoAgGe on the 1/3 and 2/3 plateaus and also captures the intriguing MR hysteresis in the ground state region where the AHE vanishes due to the P-6'm2' symmetry, since the two time-reversal partners of the ground state may have different MR. On the other hand, the difference in the small but finite orbital magnetizations of S and S' weakly lifts their degeneracy in the presence of the magnetic field in the plateau region and explains the contrasting behaviour of the hysteresis for the various field-sweep protocols discussed in detail below. We note that beyond our minimal model, there can well be other intrinsic or extrinsic mechanisms leading to the differences in these quantities in the real material, since x is not an exact symmetry operator ('Discussion'). For example, the AHC and linear magnetoconductivity in Fig. 5 are smaller than the experimental data, which may be due to considerable extrinsic contributions at low temperatures in high-quality samples, in addition to the sensitive parameter dependence of Berry-curvature-related quantities.

#### **Kinetic origin of the hysteresis**

Existence of the degenerate states in the plateau regions does not alone warrant the appearance of the hysteresis. To understand what kinetic processes enable the hysteresis and to further confirm the existence of the various plateau states, we additionally performed Hall measurements with the following sweeping and cooling protocols: (1) sweeping

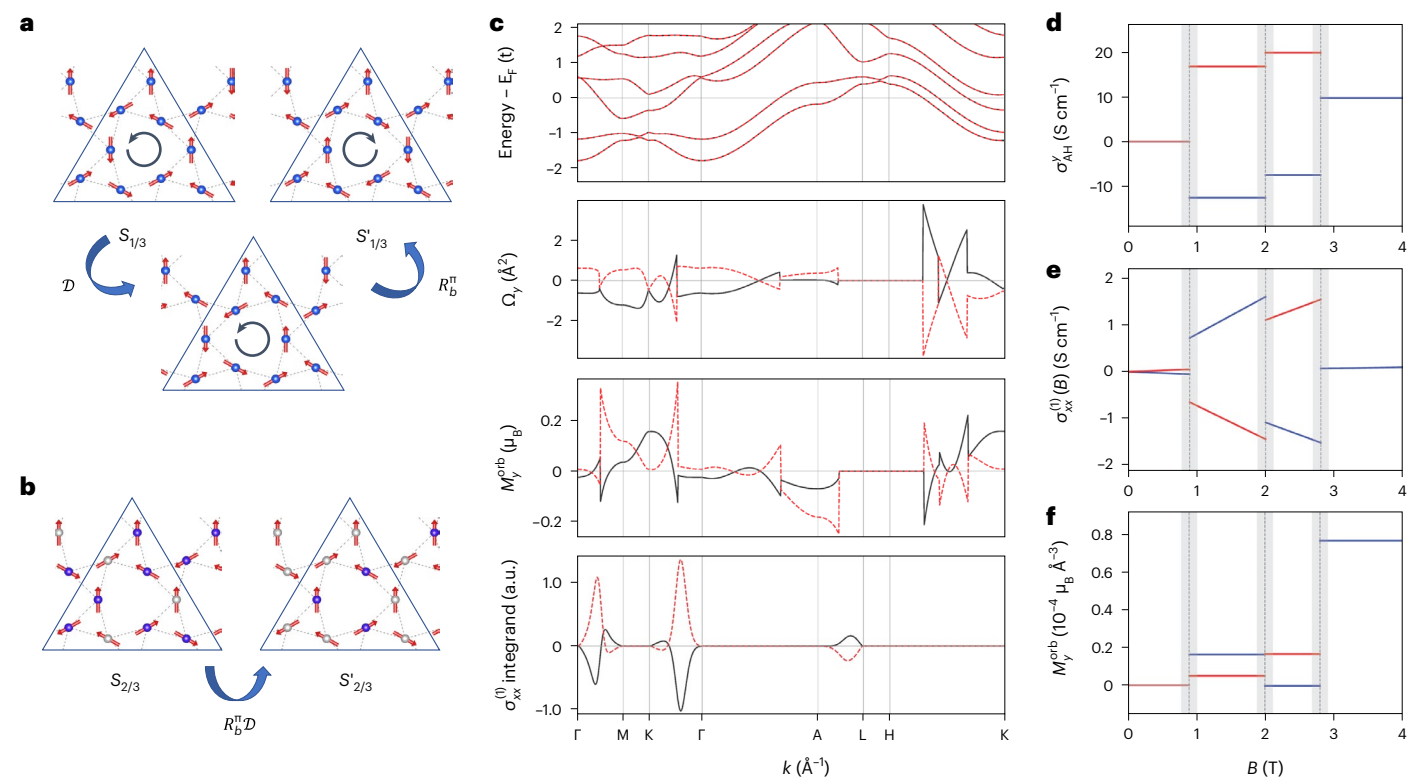


**Fig. 5** | **Model calculations for the degenerate plateau states. a**, Two degenerate states  $S_{1/3}$  and  $S'_{1/3}$  on the 1/3 plateau, connected by  $\mathcal{X} = R_b^{\mathfrak{m}} \mathcal{D}$ . **b**,  $S_{2/3}$  and  $S'_{2/3}$  on the 2/3 plateau with c-axis spin order (grey and blue spheres correspond to spins pointing into and out of the paper, respectively). **c**, Band structure and Berry-curvature-related quantities of  $S_{1/3}$  (black solid lines) and  $S'_{1/3}$  (red dashed lines). The parameter values (not fine-tuned) are  $t_v = -0.4t, \lambda_h = 0.3t, \lambda_v = 0.2t, J = -2.2t$  and  $\mu = -4.4t$ , where  $t_v, \lambda_h, \lambda_v, J$  and  $\mu$  are, respectively, nearest-neighbour out-of-plane hopping, in-plane spin-orbit

coupling, out-of-plane spin–orbit coupling, local exchange coupling and chemical potential. t is the absolute value of the nearest-neighbour hopping and is chosen as the energy unit. For orbital magnetization and linear magnetoconductivity calculations, t=1 eV.  $\mathbf{d}-\mathbf{f}$ , Intrinsic AHC ( $\mathbf{d}$ ), Berrycurvature-contributed linear magnetoconductivity ( $\mathbf{e}$ ) and orbital magnetization ( $\mathbf{f}$ ) in different plateau regions calculated using the same parameters listed above.  $\frac{\hbar}{\tau}=0.01$  eV for the results in  $\mathbf{e}$ ; x, y and z correspond to the a, b and c axes.

H between -2.5 T and +2.5 T after cooling the sample in zero field to 2 K (this protocol is denoted as SP1), (2) cooling the sample under +7 T to 2 K and sweeping between +1.3 T and +5 T, with the negative-field sweeping (for antisymmetrization; see Supplementary Note 14) done in a similar manner (denoted as SP2), (3) cooling the sample under +1.8 T to 2 K and sweeping between +0.85 T and +1.8 T, with the negative-field sweeping done in a similar manner (denoted as SP3). For the convenience of discussion, the full-range sweep between  $\pm 7$  T is denoted as SP0.

Figure 6a summarizes the Hall data obtained from the various sweep protocols. We found that SP1 and SP3 show almost no hysteresis, while SP2 shows hysteresis, albeit smaller than that of SP0. The SP3 curve coincides with that of SP1 in the contained SP3 field range. These observations, together with the other experimental facts presented above, point to the interpretations, observations and conclusions about these contrasting behaviours that are outlined in the following paragraphs and comprehensively discussed in Supplementary Note 11.

The field-cool initialization of SP3 at +1.8 T selects a state with the lowest energy out of its near-degenerate partners on the 1/3 plateau. The resulting Hall signal therefore corresponds to that of this low-energy state. That SP1 does not show hysteresis and the SP1 behaviour overlaps with that of SP3 indicates that the ground state is kinetically connected with the low-energy 1/3 plateau state or at least does not strongly favour any higher-energy 1/3 plateau states. Similarly, the low-energy 1/3 plateau state does not strongly favour any higher-energy 2/3 plateau states kinetically. However, since the SP1 and SP3 curves lie outside the hysteresis loop of SP0, the latter is expected to involve mixing of near-degenerate states.

The surprising appearance of hysteresis for SP2 suggests that the transition from the saturated state to the 2/3 plateau during the +5 T  $\rightarrow$  +1.3 T sweep strongly favours a 2/3 plateau state that is kinetically different from the lowest-energy state. Such a higher-energy 2/3 plateau state is kinetically linked to a higher-energy 1/3 plateau state, which can be explained by considering the c-axis spin order of the former (Supplementary Note 11). Consequently, during the +1.3 T  $\rightarrow +5$  T sweep, a mixture of at least two near-degenerate states appears on each of the 1/3 and 2/3 plateaus similar to that for SPO, although the composition of the mixtures may differ.

The symmetric part of the raw  $R_{ca}$  data plotted in Fig. 6b, which can be understood as an anisotropic part of the MR, additionally shows that, in contrast to SPO, SPI does not have hysteresis in the ground state region. The zero-field resistance of SPI is also smaller than that of SPO, suggesting that zero-field cooling in SPI leads to a largely uniform ground state, while in SPO the ground state region has mixing of two time-reversal partners illustrated in Fig. 1a with unequal weights. That SPI does not have hysteresis therefore means the other time-reversal partner of the ground state can only appear through a kinetic pathway involving the higher-energy 1/3 plateau states, although the detailed process is unclear because of the 1/6 plateau.

The kinetic pathways between non-collinear spin states are expected to be more complex than those of collinear magnets<sup>24,25</sup>. Future studies done with high-resolution magnetic imaging techniques will hopefully reveal more details of the phase boundaries at the metamagnetic transitions in HoAgGe. Before ending this section, we also stress that the hysteresis is not likely to be due to any remaining

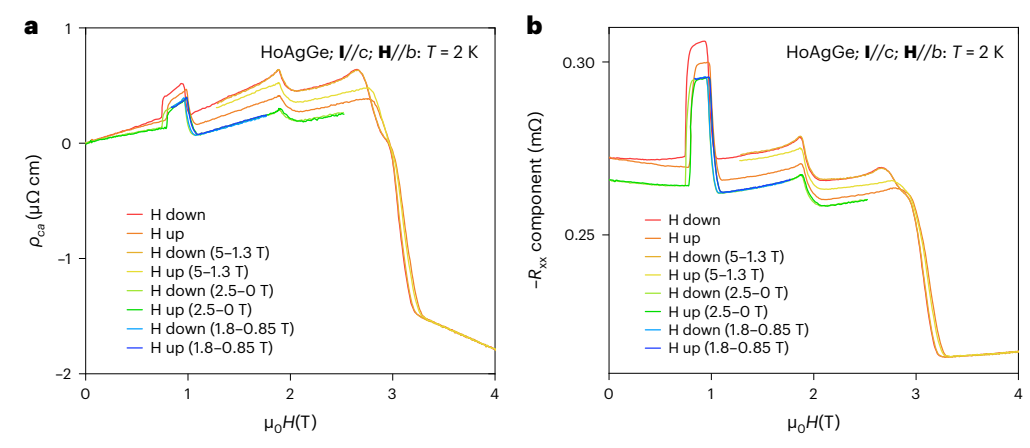


**Fig. 6** | **Hall measurements using smaller-range field sweeps. a**. The Hall resistivity  $\rho_{ca}$  of HoAgGe obtained using different field-sweep protocols under **H**//b at 2 K. **b**, The symmetric part of the raw  $R_{ca}$  signal that can be understood as an anisotropic part of the MR.

domains of a neighbouring plateau. Because the states on different plateaus have considerable differences in their net magnetization, such domains must lead to hysteresis in the magnetization curve. Such a possibility is, however, excluded by a careful quantification of the tiny magnetization hysteresis, as shown in Supplementary Fig. 26.

## Discussion

Our work shows that there can be deeper connections between near-degenerate states of frustrated spin systems, especially when there exists a natural partition of the degenerate manifold by, for example, reversing the distortion of the lattice. Conversely, since the time-reversal-like degeneracy introduced in this work is not protected by any magnetic space group symmetry, the two  $\mathcal{X}$ -partners can have different physical properties including thermodynamic, transport, optical and other properties. Such a degeneracy is an accidental or 'fragile' one for the real HoAgGe crystal, although it raises an interesting question if the band structure of the real material can also exhibit near degeneracy for the two magnetic states on the 1/3 and 2/3 plateaus, a question that can hopefully be answered by spectroscopic experiments in the future.

The consideration of c-axis spin order also leads to the question of whether there are more than two near-degenerate states in each plateau region. In Supplementary Note 8 we show that assuming the same c-axis spin order on top of  $S_{1/3}$  and  $S'_{1/3}$  increases the number of possible states to six, which can be grouped into three pairs of x-partners and the degeneracy between different pairs is not guaranteed. More generally, even if there are other possible near-degenerate states on each plateau, as long as they are not equivalent under any magnetic space group operations and can be kinetically distinguished through metamagnetic transitions, hysteretic behaviour should appear. Therefore, our picture can in principle also apply to other systems that show similar phenomena, that is, vanishing hysteresis in magnetization coexists with pronounced hysteresis in transport properties, such as  $TmB_4$  (ref. 49) and  $Pr_2Ir_2O_7$  (ref. 10). In these systems, the degeneracy when the hysteresis appears is presumably much larger since the magnetic order (or even short-range order) has not been precisely determined. It may still be possible that only a couple of low-energy or kinetically favoured states that have distinct transport properties are relevant in the field sweep, which leads to hysteresis in transport measurements.

Another issue is why the hysteresis appears above 2.5 K where the c-axis spin order comes into play, but quickly disappears near 5 K (Supplementary Fig. 30) when the plateaus are still present. One explanation for the appearance above 2.5 K is that the c-axis spin order can be stabilized by large  $\mathbf{H}//b$  through its coupling with in-plane spin

components; this surmise needs to be verified by future studies. The quick disappearance can be understood by the fact that the kinetic selection of near-degenerate states crucially relies on the competitions between the kinetic pathway, barrier, temperature and field-sweep speed. Even if the plateau states are thermodynamically stable, hysteresis will not appear if the kinetic barrier difference between the two possible final states is too small compared to the temperature scale.

In this work, with the help of electrical transport measurements in the metallic kagome ice compound HoAgGe at low temperatures, we identified an emergent time-reversal-like degeneracy between metastable ice-rule states that have virtually the same net magnetization but different magnetotransport properties. The different sizes of the various Berry-curvature-related properties of the plateau phases of HoAgGe can be traced through our minimal model to the distortion-induced Berry connection of the Bloch electrons. We expect similar phenomena should commonly appear in frustrated spin systems with non-trivial structural distortion and finite ordering wave vectors. Our study suggests a prominent potential for transport measurements in distinguishing hidden symmetries in metallic frustrated spin systems.

#### **Online content**

Any methods, additional references, Nature Portfolio reporting summaries, source data, extended data, supplementary information, acknowledgements, peer review information; details of author contributions and competing interests; and statements of data and code availability are available at https://doi.org/10.1038/s41567-023-02307-w.

# References

- Balents, L. et al. Spin liquids in frustrated magnets. Nature 464, 199–208 (2010).
- Harris, M. J. et al. Geometrical frustration in the ferromagnetic pyrochlore Ho<sub>2</sub>Ti<sub>2</sub>O<sub>2</sub>. Phys. Rev. Lett. 79, 2554–2557 (1997).
- Ramirez, A. P. et al. Zero-point entropy in 'spin ice'. Nature 399, 333–335 (1999).
- Bramwell, S. T. & Gingras, M. J. P. Spin ice state in frustrated magnetic pyrochlore materials. Science 294, 1495–1501 (2001).
- 5. Castelnovo, C., Moessner, R. & Sondhi, S. L. Magnetic monopoles in spin ice. *Nature* **451**, 42–45 (2008).
- Morris, D. J. P. et al. Dirac strings and magnetic monopoles in the spin ice Dy<sub>2</sub>Ti<sub>2</sub>O<sub>7</sub>. Science 326, 411–414 (2009).
- Fennell, T. et al. Magnetic coulomb phase in the spin ice Ho<sub>2</sub>Ti<sub>2</sub>O<sub>7</sub>.
  Science 326, 415–417 (2009).
- Hall, E. H. XVIII. On the "rotational coefficient" in nickel and cobalt. Lond. Edinb. Dublin Philos. Mag. J. Sci. 12, 157–172 (1881).

- Nagaosa, N., Sinova, J., Onoda, S., MacDonald, A. H. & Ong, N. P. Anomalous Hall effect. Rev. Mod. Phys. 82, 1539–1592 (2010).
- Machida, Y., Nakatsuji, S., Onoda, S., Tayama, T. & Sakakibara, T. Time-reversal symmetry breaking and spontaneous Hall effect without magnetic dipole order. *Nature* 463, 210–213 (2010).
- Udagawa, M. & Moessner, R. Anomalous Hall effect from frustration-tuned scalar chirality distribution in Pr<sub>2</sub>Ir<sub>2</sub>O<sub>7</sub>. Phys. Rev. Lett. 111, 036602 (2013).
- 12. Tomizawa, T. & Kontani, H. Anomalous Hall effect in the  $t_{2g}$  orbital kagome lattice due to noncollinearity: significance of the orbital Aharonov–Bohm effect. *Phys. Rev. B* **80**, 100401(R) (2009).
- Chen, H., Niu, Q. & MacDonald, A. H. Anomalous Hall effect arising from noncollinear antiferromagnetism. *Phys. Rev. Lett.* 112, 017205 (2014).
- Kübler, J. & Felser, C. Non-collinear antiferromagnets and the anomalous Hall effect. Europhys. Lett. 108, 67001 (2014).
- Nakatsuji, S., Kiyohara, N. & Higo, T. Large anomalous Hall effect in a non-collinear antiferromagnet at room temperature. *Nature* 527, 212–215 (2015).
- Nayak, A. K. et al. Large anomalous Hall effect driven by a nonvanishing Berry curvature in the noncolinear antiferromagnet Mn<sub>3</sub>Ge. Sci. Adv. 2, e1501870 (2016).
- Sürgers, C., Fischer, G., Winkel, P. & Löhneysen, H. V. Large topological Hall effect in the non-collinear phase of an antiferromagnet. *Nat. Commun.* 5, 3400 (2014).
- 18. Liu, Z. Q. et al. Electrical switching of the topological anomalous Hall effect in a non-collinear antiferromagnet above room temperature. *Nat. Electron.* **1**, 172–177 (2018).
- Zhao, K. et al. Anomalous Hall effect in the noncollinear antiferromagnetic antiperovskite Mn<sub>3</sub>Ni<sub>1-x</sub>Cu<sub>x</sub>N. Phys. Rev. B 100, 045109 (2019).
- Zhou, X. et al. Spin-order dependent anomalous Hall effect and magneto-optical effect in the noncollinear antiferromagnets Mn<sub>3</sub>XN with X = Ga, Zn, Ag, or Ni. Phys. Rev. B 99, 104428 (2019).
- Gurung, G., Shao, D.-F., Paudel, T. R. & Tsymbal, E. Y. Anomalous Hall conductivity of noncollinear magnetic antiperovskites. *Phys. Rev. Mater.* 3, 044409 (2019).
- Šmejkal, L., González-Hernández, R., Jungwirth, T. & Sinova, J. Crystal time-reversal symmetry breaking and spontaneous Hall effect in collinear antiferromagnets. Sci. Adv. 6, eaaz8809 (2020).
- Li, X., MacDonald, A. H. & Chen, H. Quantum anomalous Hall effect through canted antiferromagnetism. Preprint at https://doi.org/10.48550/arXiv.1902.10650 (2019).
- 24. Xiao, D., Chang, M.-C. & Niu, Q. Berry phase effects on electronic properties. *Rev. Mod. Phys.* **82**, 1959–2007 (2010).
- Chen, H. et al. Manipulating anomalous Hall antiferromagnets with magnetic fields. *Phys. Rev. B* 101, 104418 (2020).
- Onsager, L. Reciprocal relations in irreversible processes. II. Phys. Rev. 38, 2265 (1931).
- Xiao, C. et al. Linear magnetoresistance induced by intra-scattering semiclassics of Bloch electrons. *Phys. Rev. B* 101, 201410(R) (2020).
- 28. Wang, Y. et al. Antisymmetric linear magnetoresistance and the planar Hall effect. *Nat. Commun.* **11**, 216 (2020).
- 29. Wolf, M. & Schotte, K. D. Ising model with competing next-nearest-neighbour interactions on the Kagome lattice. *J. Phys. A: Math. Gen.* **21**, 2195–2209 (1988).
- Takagi, T. & Mekata, M. Magnetic ordering of Ising spins on Kagomé lattice with the 1st and the 2nd neighbor interactions. J. Phys. Soc. Jpn 62, 3943–3953 (1993).
- Wills, A. S., Ballou, R. & Lacroix, C. Model of localized highly frustrated ferromagnetism: the kagomé spin ice. *Phys. Rev. B* 66, 144407 (2002).

- 32. Matsuhira, K., Hiroi, Z., Tayama, T., Takagi, S. & Sakakibara, T. A new macroscopically degenerate ground state in the spin ice compound Dy<sub>2</sub>Ti<sub>2</sub>O<sub>7</sub> under a magnetic field. *J. Phys. Condens. Matter* **14**, L559 (2002).
- Tabata, Y. et al. Kagomé ice state in the dipolar spin ice Dy<sub>2</sub>Ti<sub>2</sub>O<sub>7</sub>. Phys. Rev. Lett. 97, 257205 (2006).
- Möller, G. & Moessner, R. Magnetic multipole analysis of kagome and artificial spin-ice dipolar arrays. *Phys. Rev. B* 80, 140409(R) (2009).
- 35. Chern, G.-W., Mellado, P. & Tchernyshyov, O. Two-stage ordering of spins in dipolar spin ice on the kagome lattice. *Phys. Rev. Lett.* **106**, 207202 (2011).
- Chern, G.-W. & Tchernyshyov, O. Magnetic charge and ordering in kagome spin ice. *Phil. Trans. R. Soc. A* 370, 5718–5737 (2012).
- Qi, Y., Brintlinger, T. & Cumings, J. Direct observation of the ice rule in an artificial kagome spin ice. *Phys. Rev. B* 77, 094418 (2008).
- Ladak, S., Read, D. E., Perkins, G. K., Cohen, L. F. & Branford, W. R. Direct observation of magnetic monopole defects in an artificial spin-ice system. *Nat. Phys.* 6, 359–363 (2010).
- 39. Dun, Z. L. et al. Magnetic ground states of the rare-earth tripod kagome lattice Mg<sub>2</sub>RE<sub>3</sub>Sb<sub>3</sub>O<sub>14</sub> (RE = Gd, Dy, Er). *Phys. Rev. Lett.* **116**, 157201 (2016).
- Xiao, D. et al. Berry phase correction to electron density of states in solids. *Phys. Rev. Lett.* 95, 137204 (2005).
- 41. Thonhauser, T. et al. Orbital magnetization in periodic insulators. *Phys. Rev. Lett.* **95**, 137205 (2005).
- 42. Shi, J. et al. Quantum theory of orbital magnetization and its generalization to interacting systems. *Phys. Rev. Lett.* **99**, 197202 (2007).
- Zhao, K. et al. Realization of the kagome spin ice state in a frustrated intermetallic compound. Science 367, 1218–1223 (2020).
- 44. Gopalan, V. & Litvin, D. B. Rotation-reversal symmetries in crystals and handed structures. *Nat. Mater.* **10**, 376–381 (2011).
- 45. VanLeeuwen, B. K. & Gopalan, V. The antisymmetry of distortions. *Nat. Commun.* **6**, 8818 (2015).
- 46. Li, N. et al. Low-temperature transport properties of the intermetallic compound HoAgGe with a kagome spin-ice state. *Phys. Rev. B* **106**. 014416 (2022).
- Dubovik, V. M. & Tugushev, V. V. Toroid moments in electrodynamics and solid-state physics. *Phys. Rep.* 187, 145–202 (1990).
- 48. Chen, H. Electronic chiralization as an indicator of the anomalous Hall effect in unconventional magnetic systems. *Phys. Rev. B* **106**, 024421 (2022).
- Ye, L. et al. Electronic transport on the Shastry–Sutherland lattice in Ising-type rare-earth tetraborides. *Phys. Rev. B* 95, 174405 (2017).

**Publisher's note** Springer Nature remains neutral with regard to jurisdictional claims in published maps and institutional affiliations.

Springer Nature or its licensor (e.g. a society or other partner) holds exclusive rights to this article under a publishing agreement with the author(s) or other rightsholder(s); author self-archiving of the accepted manuscript version of this article is solely governed by the terms of such publishing agreement and applicable law.

© The Author(s), under exclusive licence to Springer Nature Limited 2024

#### Methods

#### Single-crystal growth and characterization

High-quality single crystals of HoAgGe were grown using the AgGe-rich self-flux method, with typical concentration  $R_{0.06}(Ag_{0.75}Ge_{0.25})_{0.94}$  (R: Ho and Lu) (ref. 50). Mixtures were placed in a lumina crucibles and sealed in a quartz tube, heated to 1150 °C, held there for 10 h and cooled to 836 °C within 76 h, where the flux was decanted using a centrifuge.

All single crystals were characterized via X-ray diffraction with a Rigaku X'pert diffractometer using Cu  $K\alpha_1$  radiation. Magnetization measurements were performed using a vibrating sample magnetometer (Quantum Design MPMS). Electronic transport and specific heat data were obtained with Quantum Design PPMS.

#### **Demagnetization correction**

A photo of the HoAgGe crystal for Hall effect measurements is included in Supplementary Fig. 1. The b axis is perpendicular to the paper. The sample thickness is 0.45 mm, and the length along the c axis is 1.4 mm. Due to slightly different lengths of the a axis between the top and bottom surfaces, we adopt the average length of the a axis as 1.1 mm. The demagnetizing factor of this crystal is calculated by approximating it by a rectangular cuboid and using the corresponding formula in ref. 51, which yields D=0.6. The demagnetization correction is  $H_{\rm int}=H_{\rm ext}-DM$ , where D is the demagnetization factor and M is the measured magnetization. The magnetization curve labelled as A in Supplementary Fig. 2 shows the raw data, while curve B shows the result after correction for the internal demagnetizing field.

#### Thermodynamic measurements

The magnetic specific heat  $C_{\rm mag}$  data in Fig. 3 and Supplementary Fig. 5 were obtained by subtracting the contributions from Ho nuclei, lattice vibrations and itinerant electrons, as discussed in ref. 43. The ordering temperature around 7 K in Supplementary Fig. 5a is determined by the mid-point of the hump feature.

The magnetic Grüneisen parameter or adiabatic magnetocaloric effect was measured using an alternating field technique adapted to a dilution refrigerator; see ref. 52. Note that  $\Gamma_{\text{mag}} \equiv \frac{1}{T} \left( \frac{\mathrm{d} T}{\mathrm{d} \mu_0 H} \right)_S = -\frac{1}{\mu_0 \mathrm{c}} \frac{\mathrm{d} S}{\mathrm{d} H}$  which can be approximated by  $-\frac{1}{\mu_0 C_{\text{mag}}} \frac{\mathrm{d} S_{\text{mag}}}{\mathrm{d} H}$  since the non-magnetic specific heat is much smaller than the magnetic specific heat, even at 12 K, cf. Fig. 3A of ref. 43. This approximation allows us to estimate the field-dependence of magnetic entropy by integration.

## Magnetic structure refinement

Elastic single-crystal neutron-scattering details can be found in the Supplementary Materials of ref. 43. The magnetic structures are determined using Jana 2006 software  $^{53}$ .

#### Data availability

All data presented in this paper, if not present in the main text or supplementary materials, are available from the corresponding authors upon reasonable request. Source data are provided with this paper.

#### Code availability

The code for the theoretical analyses and model calculations of this study is available from the corresponding authors upon reasonable request.

#### References

- Morosan, E. et al. Thermodynamic and transport properties of RAgGe (R=Tb-Lu) single crystals. J. Magn. Magn. Mater. 277, 298–321 (2004).
- Prozorov, R. & Kogan, V. G. Effective demagnetizing factors of diamagnetic samples of various shapes. *Phys. Rev. Appl.* 10, 014030 (2018).
- Tokiwa, Y. & Gegenwart, P. High-resolution alternating-field technique to determine the magnetocaloric effect of metals down to very low temperatures. Rev. Sci. Instrum. 82, 013905 (2011).
- Petříček, V., Dušek, M. & Palatinus, L. Crystallographic Computing System JANA2006: general features. *Z. Kristallogr. Cryst. Mater.* 229, 345–352 (2014).

# Acknowledgements

We thank O. Tchernyshyov, M. Udagawa, H. Deng, I. Kezsmarki, J. Shen, H. Ren, S. Su, T. Dong and N. Wang for helpful discussions and experimental support. The work in Augsburg (K.Z., Y.T. and P.G.) was supported by the German Research Foundation (DFG) through SPP1666 (project no. 220179758), TRR80 (project no. 107745057) and TRR360 (project no. 492547816) and via the Sino-German Cooperation Group on Emergent Correlated Matter. K.Z. acknowledges the support by the National Key R&D Program of China (Grant No. 2023YFA1406003), National Natural Science Foundation of China (Grants No. 12274015), the Beijing Nova Program (Grant No. Z211100002121095), and the Fundamental Research Funds for the Central Universities. H.C. acknowledges the support by NSF CAREER grant DMR-1945023. A portion of this work was conducted at the Synergetic Extreme Condition User Facility (SECUF).

## **Author contributions**

K.Z. and P.G. proposed the experiments. K.Z. synthesized single crystals and measured magnetic properties, specific heat and electronic transport properties. Y.T. conducted magnetic Grüneisen parameter measurements. H.C. proposed the theoretical analysis and provided model calculations. K.Z., H.C. and P.G. wrote the manuscript with input from all authors.

#### **Competing interests**

The authors declare no competing interests.

#### **Additional information**

**Supplementary information** The online version contains supplementary material available at https://doi.org/10.1038/s41567-023-02307-w.

**Correspondence and requests for materials** should be addressed to K. Zhao, H. Chen or P. Gegenwart.

**Peer review information** *Nature Physi*cs thanks Hiroaki Ishizuka and the other, anonymous, reviewer(s) for their contribution to the peer review of this work.

**Reprints and permissions information** is available at www.nature.com/reprints.